ACS APPLIED NANO MATERIALS

www.acsanm.org

Article

Morphology-Dependent Charge-Separated Character in the Photoexcited States of the Photocatalytic Bismuth Oxyiodide Nanocrystals and Nanosheets: Implications for Photodynamic Therapy

Shailesh Rana, I-Hua Tsai, Kamlesh Awasthi, Sudhakar Narra, Sumit S. Bhosale, Dongling Ma, Eric Wei-Guang Diau, and Nobuhiro Ohta*

Cite This: *ACS Appl. Nano Mater.* 2025, 8, 4017−4025

Read Online

ACCESS | Metrics & More | Article Recommendations | Supporting Information

ABSTRACT: Bismuth oxyiodide (BiOI), a two-dimensional material, is well known for its photocatalytic and photovoltaic properties owing to its low bandgap, efficient charge separation, and suitable work function that facilitates various photocatalytic reactions. However, the performance of BiOI depends on the synthetic methods, as they dictate the growth directions and overall quality of the nanosheets or crystals produced. Herein, we investigated the morphology and the charge-separated character in the photoexcited states of the BiOI nanocrystals/sheets produced from alternative synthetic routes such as hydrothermal, ball milling, and hand grinding methods by using electroabsorption (E-A) spectroscopy. The optical band gaps, absorption, and E-A spectra of BiOI are shown to be sensitive to the synthetic method. The E-A spectra of BiOI nanocrystals/sheets embedded in poly(methyl methacrylate) (PMMA) matrix measured at the second harmonic of the applied field were simulated by using integral method analysis to estimate the changes in electric dipole moment and polarizability following photoexcitation. From the analysis, it is found that BiOI nanosheets prepared using a hand grinding method with a [001] orientation have much larger charge-separated character in the photoexcited states than those in the nanoparticles prepared from hydrothermal and ball milling methods with a [110] orientation, implying the excellent photoelectronic performance in BiOI nanosheets prepared by the hand grinding method in comparison with BiOI nanoparticles prepared by other methods. The present finding may open the gateway for the development of the specific BiOI material, which is suitable for photocatalysis and photodynamic therapy.

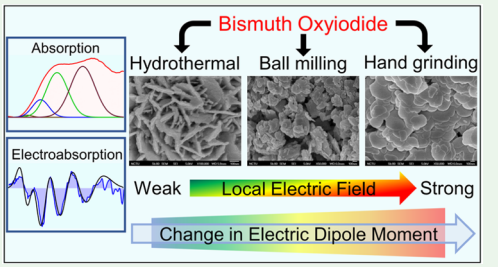

KEYWORDS: *BiOI, microspheres, nanosheets, electroabsorption, local electric field, charge transfer*

INTRODUCTION

In the pursuit of perovskite-inspired materials, bismuth oxyhalides (BiOX; X = F, Cl, Br, I) have garnered considerable attention within the scientific community due to their promising properties for optoelectronic and photocatalytic applications.[1−11] Similar to perovskites, BiOXs have metal cations with ns2 configuration that are suitable for optoelectronic applications. BiOXs are renowned for their crystalline structure, which follows the tetragonal matlockite pattern, featuring alternating layers of positively charged bismuth oxide $[Bi_2O_2]^{2+}$ and negatively charged double halide layers, resulting in a strong internal electric field, which is crucial for charge separation. The internal electric field, together with the layered structure of BiOXs, has made them attractive candidates for applications in photovoltaics, photocatalysis, photodetectors, sensing, and as anode materials in batteries.[5,6,12−25] Further, BiOXs are also relevant for photodynamic therapy.[16] As proposed in our previous work,[26] strong local field produced by charge-separated species including radical-ion pairs can induce the photodynamic action which is the basis of photodynamic therapy.

Out of the BiOX compounds, bismuth oxyiodide (BiOI) stands out as a promising option for use in photovoltaic and photocatalytic purposes due to its narrow band gap, which enables it to capture a greater amount of sunlight compared to other halides within the same family.[9,23,27−29] The growth orientations of BiOI and synthesis routes play a prominent role in these sample's optical and photocatalytic performances.[16,29−39] The internal electric field, surface potentials, and charge separation efficiency of nanosheets are often quite sensitive to the growth direction, surface terminations, and

Received: December 7, 2024
Revised: February 3, 2025
Accepted: February 7, 2025
Published: February 13, 2025

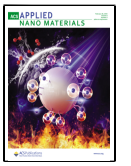

https://doi.org/10.1021/acsanm.4c06892
ACS Appl. Nano Mater. 2025, 8, 4017−4025

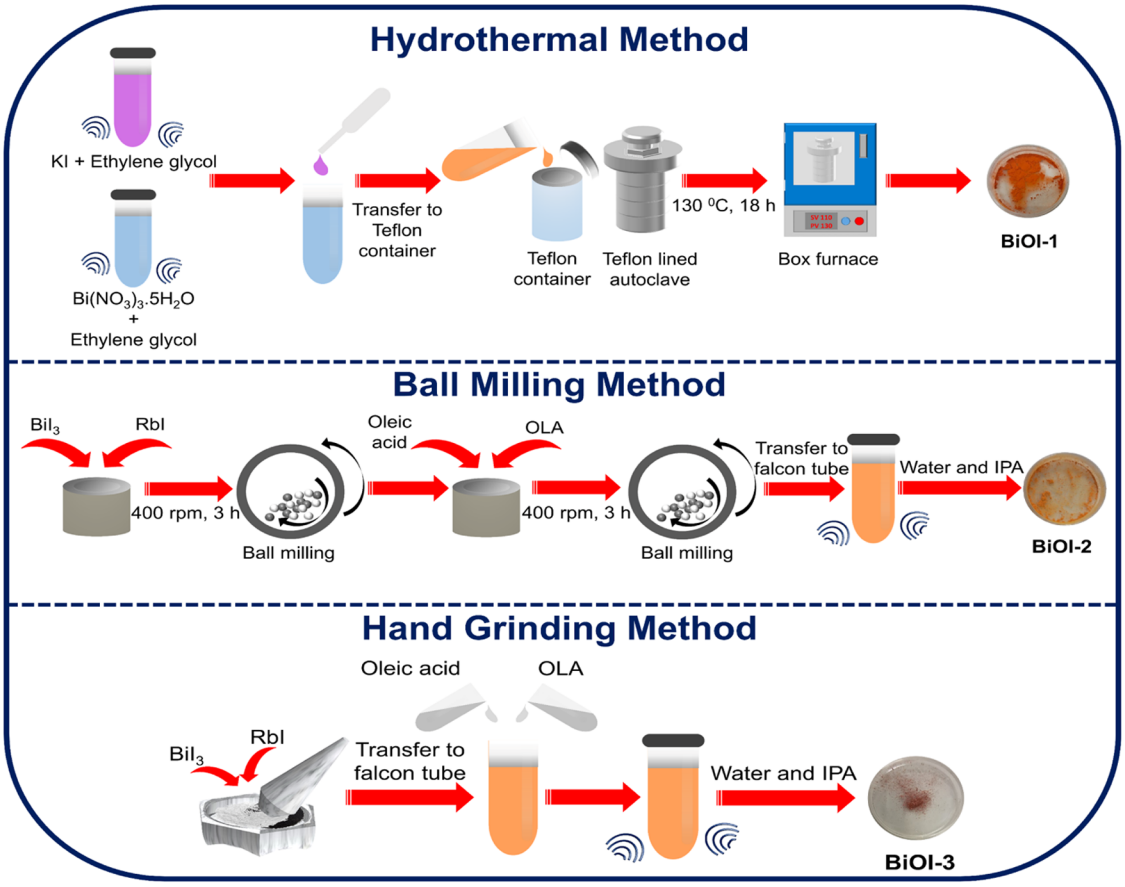

Figure 1. Synthesis routes of bismuth oxyiodide powders.

defect densities. The photocatalytic performance of BiOXs is notably influenced by their optical properties, which can be altered through external factors like strain and electric fields.[13,14,40,41] Moreover, Barhoumi et al.[41] conducted ab initio calculations and found that applying an external transverse electric field to BiOXs led to a reduction in their band gap. Additionally, they observed a transition from a semiconductor to a metal when subjected to a strong field exceeding 0.5 V/Å. Thus, it is essential to understand the fundamental electronic properties of BiOXs in photoexcited states to counter the obstacles to their advancement.

Extensive research on BiOX materials has consistently shown the pivotal role of surface area in governing catalytic performance. BiOXs with inherently high surface areas provide more active sites for surface-mediated processes, such as charge transfer and adsorption, thereby augmenting their overall catalytic efficiency.[31,42,43] Beyond the surface area, the orientation of crystal planes has been shown to influence catalytic performance significantly. Notably, BiOX materials exhibiting relatively smaller surface areas but preferentially exposed [001] crystal planes have demonstrated high catalytic activity.[44−49] This enhanced performance is attributed to the internal electric field along the [001] direction, which facilitates more efficient charge separation. The synergistic interplay between the intrinsic properties of the [001] orientation and the overall material design highlights the critical role of crystal plane engineering in optimizing the functionality of the BiOX materials. Inspired by these studies, we aim to explore the properties of photoexcited states of BiOI nanocrystals and nanosheets with varying surface orientations using electroabsorption (E-A) spectroscopy. E-A spectroscopy, a powerful technique that measures the electric field-induced changes in absorption spectra, provides valuable insights into the nature of excited states by evaluating changes in electric dipole moment ($\Delta\mu$) associated with the charge separation character upon photoexcitation. This makes E-A spectroscopy an ideal tool for probing charge separation dynamics, a key factor in understanding and optimizing the material's optoelectronic applications. To the best of our knowledge, this is the first report of E-A studies of BiOX materials.

In this work, we present the E-A spectra of BiOI films grown from the hydrothermal, ball milling, and hand grinding methods. The shapes and magnitudes of the E-A spectra and the estimated molecular properties, such as the changes in electric dipole moment and polarizability following photoexcitation, were shown to be sensitive to the synthetic routes and morphology of the sample. The BiOI nanosheets prepared from the hand grinding method with a [001] orientation are shown to display exemplary optical characteristics compared to those prepared from hydrothermal and ball milling methods with [110] orientations. The present study emphasizes the structure-dependent electronic properties of BiOI nanocrystals and nanosheets. The large estimated value of $\Delta\mu$ for BiOI nanosheets with [001] orientations may have a potential application for photodynamic therapy, as their efficient charge separation can generate large electric fields, which can enhance the generation of reactive species of oxygen in biological system.[26]

https://doi.org/10.1021/acsanm.4c06892
ACS Appl. Nano Mater. 2025, 8, 4017−4025

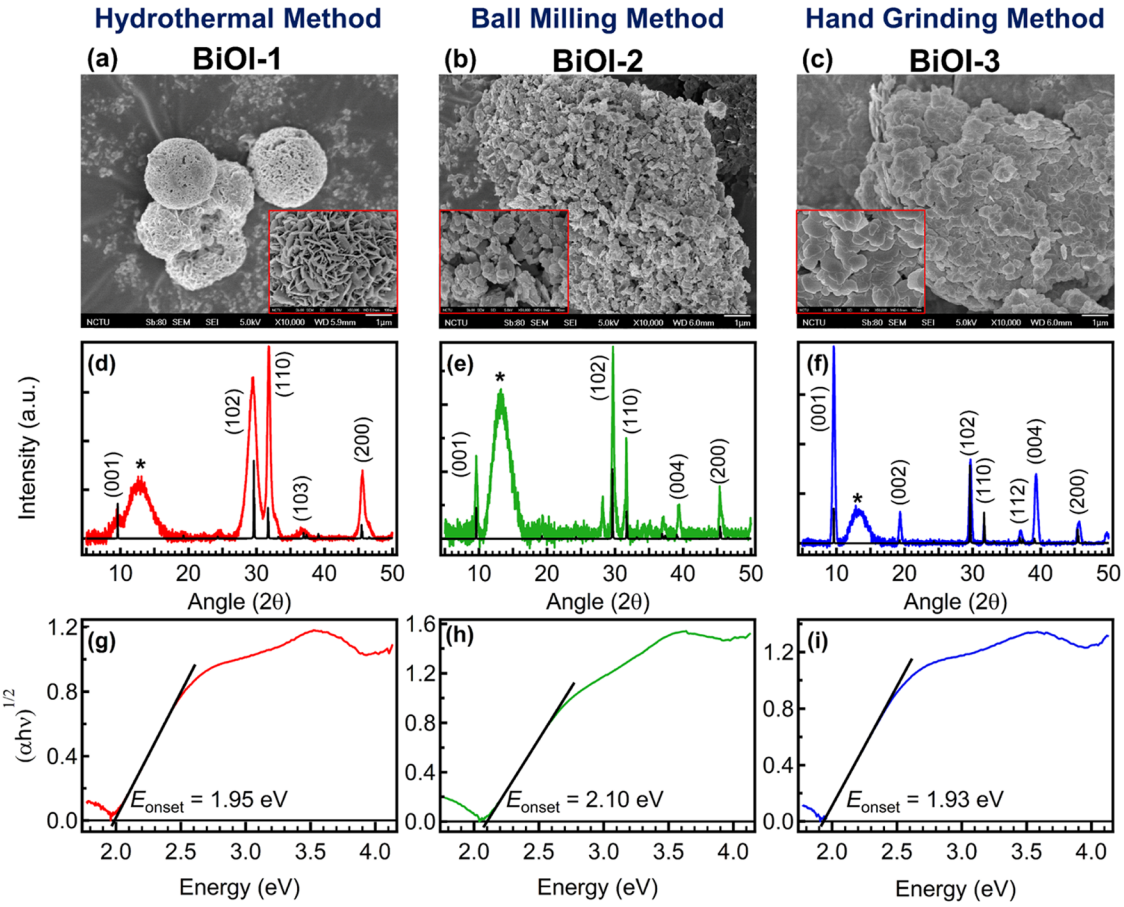

Figure 2. (a–c) Scanning electron micrographs (scale bars are 1 μm and 100 nm (inset)), (d–f) X-ray diffraction patterns (* substrate signal) with Crystallographic Information File (CIF),[17] and (g–i) Tauc plots obtained from the UV–vis absorption spectra of BiOI samples synthesized from the hydrothermal, ball milling, and hand grinding methods (from left to right).

RESULTS AND DISCUSSION

BiOI samples used in the study were synthesized using three methods: hydrothermal method, ball milling, and hand grinding, as shown in Figure 1. BiOI was prepared directly from the reaction between the potassium iodide and bismuth nitrate in ethylene glycol solvent in the hydrothermal method. In ball milling and hand grinding methods, on the other hand, BiOI was prepared via an indirect route by synthesizing a bismuth-based triple perovskite from precursors of bismuth iodide, rubidium iodide and turning the triple perovskite to the desired product via a hydrolysis reaction using water and isopropanol as solvents. The detailed synthesis procedures of BiOI are presented in the Experimental Methods section. Hereafter, the BiOI samples synthesized using hydrothermal, ball milling, and hand grinding methods are labeled BiOI-1, BiOI-2, and BiOI-3, respectively.

The synthesized samples were further characterized using scanning electron microscopy (SEM), X-ray diffraction (XRD), and UV–vis absorption spectroscopy to examine the morphological, structural, and optical characteristics of the samples and to identify the differences among these three synthetic methods. The SEM micrographs presented in Figures 2a–c and S1 show that the morphology of the BiOI samples is quite sensitive to the synthetic methods. From SEM images (Figures 2 and S1), the BiOI-1 sample exhibits a flower-like microsphere structure composed of interconnected nanosheets. In contrast, BiOI-2 displays irregularly oriented nanosheet structures, while BiOI-3 shows a morphology characterized by regularly stacked nanosheets. The average particle sizes of BiOI-1, BiOI-2, and BiOI-3 are approximately 2.6 μm, 120 nm, and 220 nm, respectively. The purity of the synthesized BiOI samples was examined with energy-dispersive X-ray (EDX) analysis (Figure S2), which confirmed their excellent purity, with only trace amounts of potassium (K) and rubidium (Rb). In the EDX analysis of all three samples, the O content was observed to be higher than that of Bi and I. This is likely attributed to the presence of surface-absorbed oxygen from carbon tape, which we used to affix the BiOI samples for SEM imaging and EDX analysis. As shown in Figure 2d–f, the XRD pattern of BiOI samples is similar to the tetragonal phase described elsewhere.[21,33,50] However, it is noticed that the relative orientations and peak intensities depend on the synthetic route. The BiOI-1 and BiOI-2 samples showed orientations with (102) and (110) having slight changes in their relative intensities between these two samples, whereas the BiOI-3 sample showed a characteristic low-angle peak, which might correspond to (001). The observed low-angle peak and the sheet-like morphologies in BiOI-3 samples corroborate well with each other. The absorption spectra of BiOI samples cover the visible and UV regions between 2 and 4 eV, as shown in Figure 2g–i. However, the band gaps, absorption profiles, and band-edge steepness displayed sensitivity to the synthetic routes. The band gaps of the synthesized BiOI-1, BiOI-2, and BiOI-3 samples estimated from the Tauc plot are 1.95, 2.10, and 1.93 eV, respectively, as

https://doi.org/10.1021/acsanm.4c06892
ACS Appl. Nano Mater. 2025, 8, 4017–4025

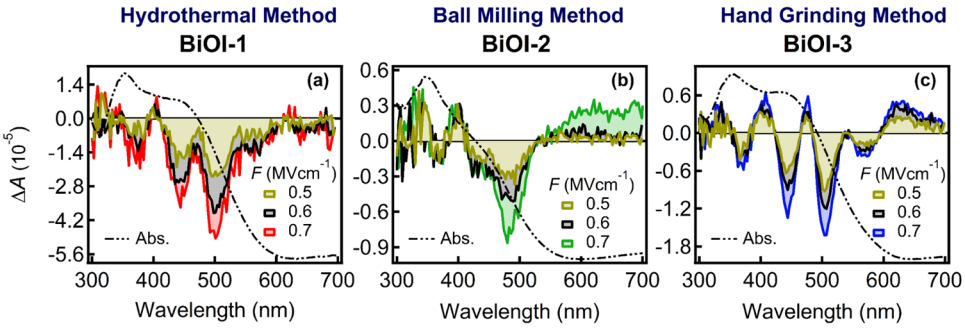

Figure 3. E-A spectra of BiOI/PMMA samples measured at the second harmonic of the frequency of applied electric field with a modulation frequency of 1 kHz for BiOI-1 (a), BiOI-2 (b), and BiOI-3 (c). The chain lines show the absorption spectra.

shown in Figure 2g–i, which are within the range of reported values.[8,51] It is worth mentioning that the bandgaps of BiOI crystals are known to be sensitive to synthetic routes and sample thickness.[8,51]

The field-induced changes in the absorption spectra of BiOI devices, i.e., the so-called electroabsorption (E-A) spectra, were obtained by measuring transmitted light intensity synchronized at the second harmonic frequency of the applied sinusoidal wave having a frequency of 1 kHz and field strengths varied between 0.4 and 0.7 MV cm^{-1}, as shown in Figure 3. The BiOI devices were prepared by spin coating toluene solution of BiOI in PMMA matrix on an ITO-coated (back electrode) glass substrate, and an ∼15 nm thick semitransparent aluminum (front electrode) layer was deposited atop to complete the device fabrication. E-A spectra of BiOI/PMMA samples showed multiple bands, which are very different from the steady-state absorption spectra, as shown in Figures 3 and S3. The E-A signal intensity increased with increasing applied field strength, as shown in Figure 3; the absorption variation (ΔA) magnitudes were proportional to the square of the applied field strength (F), as shown in Figure S3. The E-A spectra of BiOI-1/PMMA and BiOI-3/PMMA samples show four depletion bands, whereas three depletion bands are identified in the BiOI-2/PMMA sample. Moreover, BiOI-2/PMMA samples showed field-induced changes in absorption in the sub-bandgap region between 600 and 700 nm, which might be due to some contribution from trap states. The peak positions of BiOI-2/PMMA sample show a blue shift with broadened bands compared to BiOI-1/PMMA and BiOI-3/PMMA samples. Despite the similarities in the spectral profiles of BiOI-1/PMMA and BiOI-3/PMMA samples, they showed slight variations in the relative intensity ratios between the bands and bandwidths, probably due to the presence of sub-bandgap states.

Typically, E-A spectra are characterized by the change in peak intensity, shift (red or blue), and line width of the absorption spectrum ($A(\nu)$) due to the influence of the applied electric field (F_A), leading to the formation of the zeroth, first, and second derivatives of $A(\nu)$, respectively. According to the theory of E-A spectroscopy, the change in absorbance (ΔA) affected by F_A can be expressed as a linear combination of the zeroth, first, and second derivatives of $A(\nu)$, i.e., by the following equation:[52−56]

$$\Delta A = (fF_A)^2\left[aA(\nu) + b\nu\frac{d}{d\nu}\left(\frac{A(\nu)}{\nu}\right) + c\nu\frac{d^2}{d\nu^2}\left(\frac{A(\nu)}{\nu}\right)\right] \quad (1)$$

In eq 1, f and F_A denote the internal field factor and magnitude of the applied electric field, respectively. The coefficients "a", "b", and "c" depend on the field-induced changes in the transition moment, spectral shift (due to the change in polarizability following photoexcitation, $\Delta\alpha$), and spectral broadening of absorption (due to the change in electric dipole moment following photoexcitation, $\Delta\mu$), respectively. The differential form of the E-A spectrum represented by eq 1 is a valuable tool to simulate the E-A spectrum when the corresponding absorption bands are known. However, the absorption bands in semiconductors or two-dimensional materials are often buried under a large continuum background and/or a plural number absorption bands overlap, resulting in the broad absorption bands. In such a case as the present one, analysis by using eq 1 is too complicated, and the integral method was shown to be powerful to analyze the E-A spectra and identify the absorption bands buried under the broad background or overlapped with other absorption bands.[57−59] In the integral method analysis, eq 1 is integrated twice, and the resulting expressions for the first and second integrals of eq 1 given by the following equations can be used to check the simulation of the E-A spectra:

$$\int \Delta A(\nu)\mathrm{d}\nu \simeq (fF)^2\left[a\int A(\nu)\mathrm{d}\nu + bA(\nu) + c\frac{\mathrm{d}A(\nu)}{\mathrm{d}\nu}\right] \quad (2)$$

$$\int\left\{\int \Delta A(\nu)\mathrm{d}\nu\right\}\mathrm{d}\nu \simeq (fF)^2\left[a\int\left\{\int A(\nu)\mathrm{d}\nu\right\}\mathrm{d}\nu + b\int A(\nu)\mathrm{d}\nu + cA(\nu)\right] \quad (3)$$

If the absorption spectrum of each band, i.e., $A(\nu)$, shows a Gaussian profile, the first integral of $A(\nu)$ in eqs 2 and 3 shows a monotonic increase or decrease, depending on the sign of the coefficient a and b, respectively, with increasing excitation energy and shows saturation in the high-energy region, while the second integral of $A(\nu)$ in eq 3 shows just monotonic increase or decrease, depending on the positive or negative sign of a, without saturation. When the second integral of $\Delta A(\nu)$ is watched from this point of view, the absorption peak which gives a large contribution of the second derivative term in eq 1 is considered to show a peak in the second integral of $\Delta A(\nu)$, caused by the third term on the right of eq 3. The second integral spectra of the E-A spectra of BiOI-1, BiOI-2, and BiOI-3 are shown in Figure 4, and four peaks identified from the change of slope are indicated in the second integral

https://doi.org/10.1021/acsanm.4c06892
ACS Appl. Nano Mater. 2025, 8, 4017−4025

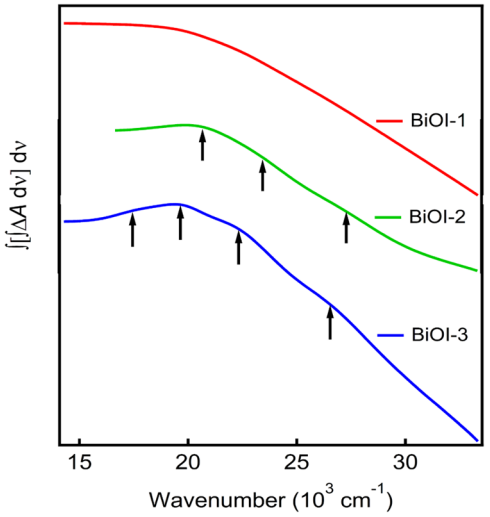

Figure 4. Second integral spectra (shape) of ΔA of BiOI-1, 2, and 3 (from top to bottom). The arrows show the identified peaks from the change of slope.

plot of BiOI-3. Then, the E-A spectra of BIOI-3 have been analyzed by assuming the presence of four absorption bands having a Gaussian profile in this region (G1−G4) and by using the integral method. The location of G1−G4 of BiOI-3 is shown in Table S1, i.e., G1 (17,544 cm^{-1}, 2.18 eV), G2 (19,646 cm^{-1}, 2.44 eV), G3 (22,326 cm^{-1}, 2.77 eV), and G4 (26,537 cm^{-1}, 3.29 eV). Rieger et al.[60] presented analogous findings of four distinctive optical transitions (2.30, 2.55, 2.87, and 3.35 eV) due to phase space filling of closely spaced levels of the valence band at the Γ point of the Brillouin zone following photoexcitation in BiOI nanoplatelets at a low temperature (4 K), by using femtosecond differential transmission spectroscopy. The positions of G1−G4 estimated from the integral spectra of the E-A spectra of BiOI-3 are very close to the ones reported by Rieger et al. In the second integral spectra, three faint peaks can be identified in BiOI-2, but a clear peak cannot be identified in BiOI-1. These results imply that the contribution of the second derivative term in eq 1 is much smaller in BiOI-1 and BiOI-2 than in BiOI-3, that is, the magnitude of the change in electric dipole moment following absorption is much larger in BiOI-3 than the others. As in the case of BiOI-3, the E-A spectra of BiOI-1 and BiOI-2 have also been analyzed by assuming the presence of four absorption bands in this region with trial and error, since the absorption spectra of these compounds are quite similar to each other, as shown in Figure 5, where the E-A spectra, their first and second integral spectra, and simulated spectra are also shown. The first and second integral spectra and their simulations with

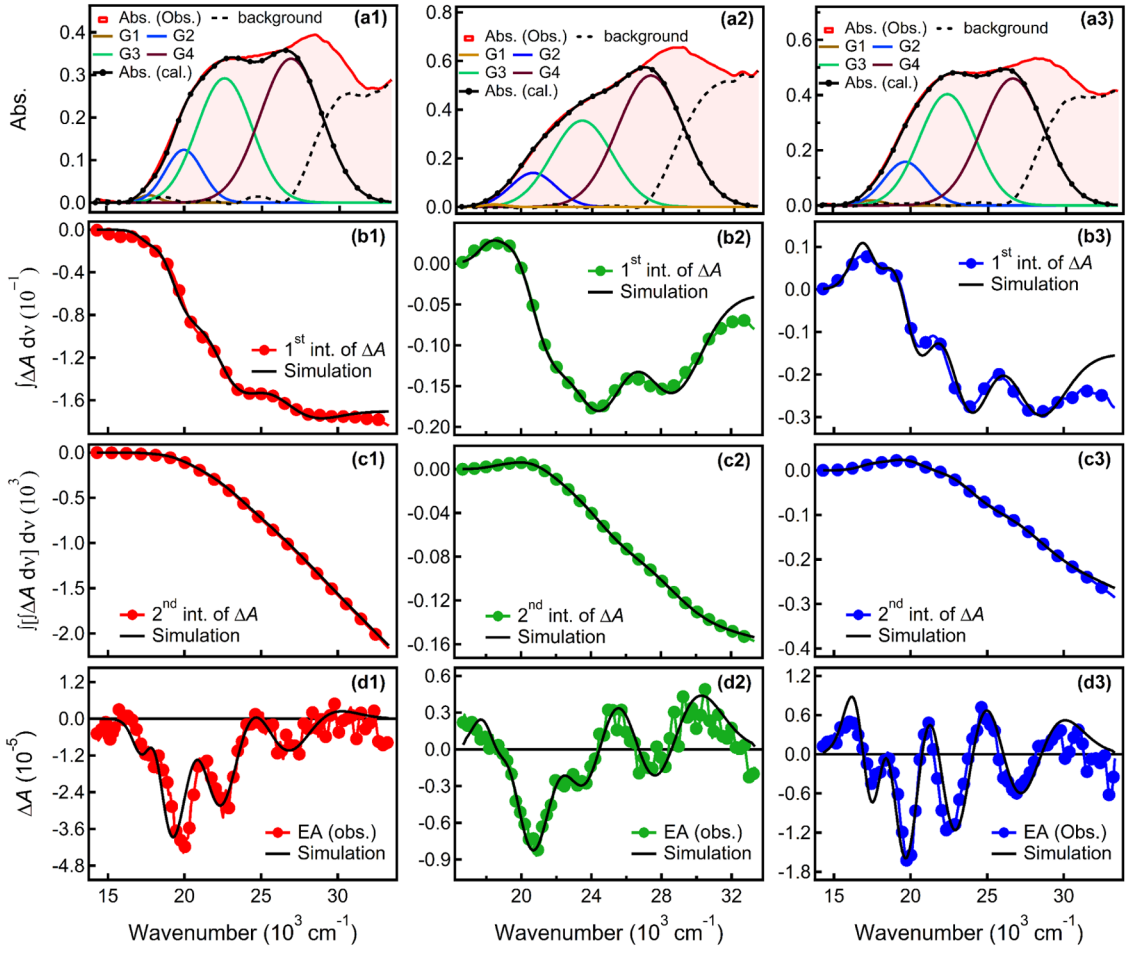

Figure 5. Integral method analysis of the E-A spectra of BiOI-1/PMMA, BiOI-2/PMMA, and BiOI-3/PMMA films (from left to right). (a) Absorption spectra, (b) the first integral of the E-A spectra, (c) the second integral of the E-A spectra, and (d) the E-A spectra of BiOI-1, 2, and 3. The simulated spectra are also shown in the figure.

https://doi.org/10.1021/acsanm.4c06892
ACS Appl. Nano Mater. 2025, 8, 4017−4025

derivative and integral contributions of absorption Gaussian bands are shown in Figure S4.

The parameters obtained from the fitting, that is, not only the peak positions of G1−G4, but also the bandwidth of these bands, coefficients *a*, *b*, *c* in eq 1, as well as the estimated magnitudes of the change in electric dipole moment ($\Delta\mu$) and polarizability ($\Delta\alpha$) following photoexcitation into these four bands are shown in Tables S1 and S2. The magnitudes of $\Delta\mu$ estimated for the G1−G4 bands of BiOI/PMMA composites obtained from the fitting coefficients are shown in Figure 6.

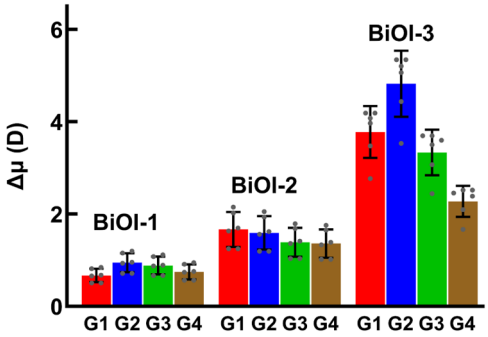

Figure 6. Statistically analyzed changes in $\Delta\mu$ of BiOI-1/PMMA, BiOI-2/PMMA, and BiOI-3/PMMA films for Gaussian bands G1, G2, G3, and G4. The results are presented as mean ± SD.

The internal electric field caused by electric dipole moment may play a significant role in charge separation following photoexcitation, since the charge-separated species can produce local electric field to the surroundings.[61] Therefore, the magnitudes of $\Delta\mu$ following photoexcitation, which are probably associated with the structural and morphological characteristics, may give an insight into associated photovoltaic and photocatalytic performances in BiOI nanocrystal/sheets.

As shown in Figure 6, the G2 band, which is close to the band edge, shows a large value of $\Delta\mu$, compared to the bands higher and lower in energy, suggesting a large charge separation following photoexcitation limited to a very narrow region. Further, the magnitude of $\Delta\mu$ at the G2 band of BiOI-3 is much larger than the others, as expected from the second integral of the E-A spectra, compared with the others. Theoretical calculations on bismuth oxyhalides propose that molecules with dipole moments larger than 2 debye can undergo charge separation efficiently and are suitable for photocatalytic and photovoltaic applications.[62,63] In that sense, BiOI-3 is considered to show a much more efficient photocatalytic performance than others; the BiOI samples prepared from the hand grinding method can undergo charge separation more efficiently than the hydrothermal and ball milling methods.

The BiOI-1 crystals prepared by the hydrothermal method produced a spheroid shape with a flowery texture, and BiOI-2 crystals prepared by the ball milling method produced an irregular sheet-like structure with random orientations. On the contrary, the morphology of BIOI-3 crystals prepared by the hand grinding method showed a two-dimensional sheet-like structure, as shown in Figure 2. The XRD pattern also reveals that the orientation of the [001] plane follows the trend BiOI-3 > BiOI-2 > BiOI-1, which aligns with the trend of $\Delta\mu$ estimated from the analysis of E-A spectra. The large value of $\Delta\mu$ in BiOI-3 leading to a generation of a strong internal field indicates that a remarkable dipolar state is produced on the sheet by photoexcitation of BiOI-3. The large local electric fields are considered to play a prominent role in enhancing the charge transfer efficiencies of materials.[14,27,64,65] The present results suggest that the strong internal electric fields generated by photoirradiation, which play a significant role in the charge transport properties of the BiOI samples, depend on the fabrication method, thereby highlighting the potential of both the sample and the E-A spectroscopy technique. The fact that layered BiOI nanomaterials are relevant also for photodynamic therapy may be also due to the presence of strong local fields produced by photoirradiation.[16]

CONCLUSIONS

In this work, we showed that BiOI nanocrystals/sheets synthesized from hydrothermal, ball milling, and hand grinding methods display different morphologies with slight variations in the absorption profiles and optical bandgaps. The optical bandgaps estimated from the Tauc plots are 1.95, 2.10, and 1.93 eV, respectively, for BiOI-1, BiOI-2, and BiOI-3 samples. The E-A spectra BiOI show four distinct transitions buried under the broad absorption profile of these samples. The changes in dipole moments and polarizabilities estimated by simulating the E-A spectra with the integral method show that charge separation is very efficient in a narrow region of the optical transition associated with the G2 band, implying a limitation of the optical performance of these samples. The charge separation efficiency was shown to be highest for the BiOI sample with a sheet-like structure, prepared from the hand grinding method, i.e., BiOI-3, with [001] orientation owing to the large changes in dipole moment, compared with the samples prepared from the hydrothermal and ball milling methods with [110] orientation. The present results provide experimental evidence of the need to grow sheet-like structures, which can have dipolar states following photoexcitation, to harvest charges efficiently, in contrast to nondirectional or spheroid-like structures. The present finding may open the gateway for the development of the specific BiOI material which is suitable for photocatalysis and photodynamic therapy.

EXPERIMENTAL METHODS

Materials. All materials were used without purification: bismuth nitrate pentahydrate ($Bi(NO_3)_3{\cdot}5H_2O$, 98%, AlfaAesar) bismuth iodide (B_3, 99%, Sigma-Aldrich), rubidium iodide (RbI, 99%, Sigma-Aldrich), 2-propanol (IPA, 99%, Sigma-Aldrich), oleylamine (OLA, technical grade, 70%, Sigma-Aldrich), oleic acid (OA, technical grade, 90%, Sigma-Aldrich), and toluene (anhydrous, 99.8%, Sigma-Aldrich).

Synthesis of BiOI. We synthesized BiOI using three different methods: hydrothermal, ball milling, followed by sonication, and hand grinding, followed by sonication. The resulting BiOI samples are termed BiOI-1, BiOI-2, and BiOI-3, respectively.

BiOI-1. $Bi(NO_3)_3{\cdot}5H_2O$ (6 mmol) and KI (6 mmol) were separately dissolved in ethylene glycol (50 mL) in two falcon tubes. Both solutions were sonicated for 30 min. Subsequently, the KI solution was added dropwise to the $Bi(NO_3)_3{\cdot}5H_2O$ solution. Once both solutions were mixed completely, the resulting mixture was transferred into a Teflon cage autoclave and heated at 130 °C for 18 h in the muffle furnace. After cooling down the autoclave reactor to room temperature, the solid material was separated and washed with deionized water and ethanol to remove the inorganic ions and remaining ethylene glycol. The final output product was dried and stored for further use.

BiOI-2. RbI (612 mg) and BiI_3 (568 mg) were transferred into the ball milling holder and ground for 3 h at 400 rpm, with intervals of 50

https://doi.org/10.1021/acsanm.4c06892
ACS Appl. Nano Mater. 2025, 8, 4017−4025

s on and 10 s off. After this initial grinding, 40 mL of oleic acid and 5 mL of oleylamine were added, and the mixture was ground for another 3 h under the same conditions. The resulting mixture was then transferred to a falcon tube and sonicated for 4 days. Subsequently, the mixture was centrifuged and the supernatant was discarded. Toluene was added to the solid residue and sonicated for 30 min. After centrifugation, the solid precipitate was dispersed in 20 mL of IPA and 2 mL of deionized water and sonicated for 1 h. Finally, the solution was centrifuged once more to collect the final precipitate, which constituted the BiOI product.

BiOI-3. BiOI was synthesized by grinding BiI_3 and RbI together in an agate mortar inside the glovebox. After grinding, the mixture was transferred to a falcon tube with oleic acid (40 mL) and oleylamine (4 mL). This mixture was then sonicated for 4 days. Following sonication, the solution mixture was washed with toluene to remove excess ligands. The resulting solid precipitate was dispersed in IPA and deionized water and sonicated for 30 min. Finally, the solution was centrifuged, and the solid BiOI precipitate was collected and dried for further use.

Device Fabrication. The synthesized BiOI powder (0.03 g) and PMMA (0.05 g) were mixed in 1 mL of toluene under continuous stirring for 12 h to prepare the solid thin film for E-A measurement. The toluene solution having BiOI and PMMA was kept at rest for a little time to settle down the large particles and then spin-coated at 350 rpm for 30 s on an ITO-coated glass substrate. For spin coating, we carefully took the solution from the top to avoid the large particles. Subsequently, a semitransparent ∼15 nm thick layer of aluminum (Al) was thermally deposited onto the surface of BiOI/PMMA. The conductive ITO and Al layers were used as electrodes for the E-A measurements.

Characterizations. The thickness of the fabricated film, measured at 0.6 μm, was recorded by an α step profiler (Veeco Dektak 150), within ∼10% deviation. The thickness determination facilitated evaluation of the applied field strength (F_A). The X-ray diffraction patterns of BiOI samples were recorded from a Bruker D8 Advance diffractometer. The UV−vis absorption spectra of BiOI samples were measured using a JASCO spectrometer. The scanning electron microscopic images of BiOI samples were measured using a Hitachi SU8010. The E-A spectra presented in this study were obtained by the spectrometer (FP777, JASCO) whose information can be found in our previous studies.[66,67] Briefly, a sinusoidal alternating current (AC) voltage with a frequency of 1 kHz was applied to the sample. The field-induced change in transmitted light intensity (ΔI_T) was detected at the second harmonic (2Ω) of the modulation frequency of the applied voltage by using a lock-in amplifier. The E-A signal, that is, the field-induced change in absorbance (ΔA), was determined from $\left(-\frac{2\sqrt{2}}{\ln 10}\frac{\Delta I_T(2\Omega)}{I_T}\right)$.

■ ASSOCIATED CONTENT

Supporting Information

The Supporting Information is available free of charge at https://pubs.acs.org/doi/10.1021/acsanm.4c06892.

SEM images, EDX analysis, field strength dependence on E-A signals, first and second integrals of E-A spectra and their analysis, fitting parameters of Gaussian bands to simulate the E-A spectra, fitting parameters of the E-A spectra, and magnitudes of $\Delta\mu$ and $\Delta\alpha$ (PDF)

■ AUTHOR INFORMATION

Corresponding Author

Nobuhiro Ohta − *Department of Applied Chemistry and Institute of Molecular Science, National Yang Ming Chiao Tung University, Hsinchu 300093, Taiwan; Center for Emergent Functional Matter Science, National Yang Ming Chiao Tung University, Hsinchu 300093, Taiwan;* orcid.org/0000-0003-4255-6448; Email: nohta@nycu.edu.tw

Authors

Shailesh Rana − *Department of Applied Chemistry and Institute of Molecular Science, National Yang Ming Chiao Tung University, Hsinchu 300093, Taiwan;* orcid.org/0000-0002-4349-101X

I-Hua Tsai − *Department of Applied Chemistry and Institute of Molecular Science, National Yang Ming Chiao Tung University, Hsinchu 300093, Taiwan*

Kamlesh Awasthi − *Department of Applied Chemistry and Institute of Molecular Science, National Yang Ming Chiao Tung University, Hsinchu 300093, Taiwan; Center for Emergent Functional Matter Science, National Yang Ming Chiao Tung University, Hsinchu 300093, Taiwan;* orcid.org/0000-0001-7852-059X

Sudhakar Narra − *Department of Applied Chemistry and Institute of Molecular Science, National Yang Ming Chiao Tung University, Hsinchu 300093, Taiwan; Center for Emergent Functional Matter Science, National Yang Ming Chiao Tung University, Hsinchu 300093, Taiwan;* orcid.org/0000-0003-4893-9204

Sumit S. Bhosale − *Center Énergie Matériauxet Télécommunications, Institut National de la Recherche Scientifique (INRS), Varennes, Quebec J3X 1P7, Canada;* orcid.org/0009-0004-6763-2712

Dongling Ma − *Center Énergie Matériauxet Télécommunications, Institut National de la Recherche Scientifique (INRS), Varennes, Quebec J3X 1P7, Canada;* orcid.org/0000-0001-8558-3150

Eric Wei-Guang Diau − *Department of Applied Chemistry and Institute of Molecular Science, National Yang Ming Chiao Tung University, Hsinchu 300093, Taiwan; Center for Emergent Functional Matter Science, National Yang Ming Chiao Tung University, Hsinchu 300093, Taiwan;* orcid.org/0000-0001-6113-5679

Complete contact information is available at: https://pubs.acs.org/10.1021/acsanm.4c06892

Notes

The authors declare no competing financial interest.

■ ACKNOWLEDGMENTS

This work was supported by National Science and Technology Council in Taiwan (NSTC 113-2113-M-A49-021). This work was also supported by the Center for Emergent Functional Matter Science of National Yang Ming Chiao Tung University from The Featured Areas Research Center Program within the framework of the Higher Education Sprout Project by Ministry of Education in Taiwan.

■ REFERENCES

(1) Hoye, R. L. Z.; Schulz, P.; Schelhas, L. T.; Holder, A. M.; Stone, K. H.; Perkins, J. D.; Vigil-Fowler, D.; Siol, S.; Scanlon, D. O.; Zakutayev, A.; Walsh, A.; Smith, I. C.; Melot, B. C.; Kurchin, R. C.; Wang, Y.; Shi, J.; Marques, F. C.; Berry, J. J.; Tumas, W.; Lany, S.; Stevanović, V.; Toney, M. F.; Buonassisi, T. Perovskite-Inspired Photovoltaic Materials: Toward Best Practices in Materials Characterization and Calculations. *Chem. Mater.* **2017**, *29* (5), 1964−1988.

(2) Pecunia, V.; Zhao, J.; Kim, C.; Tuttle, B. R.; Mei, J.; Li, F.; Peng, Y.; Huq, T. N.; Hoye, R. L. Z.; Kelly, N. D.; Dutton, S. E.; Xia, K.; MacManus-Driscoll, J. L.; Sirringhaus, H. Assessing the Impact of Defects on Lead-Free Perovskite-Inspired Photovoltaics via Photo-

induced Current Transient Spectroscopy. *Adv. Energy Mater.* **2021**, *11* (22), No. 2003968.
(3) Lv, X.; Lam, F. L. Y.; Hu, X. A Review on Bismuth Oxyhalide (BiOX, X = Cl, Br, I) Based Photocatalysts for Wastewater Remediation. *Front. Catal.* **2022**, *2*, No. 839072.
(4) Yang, Y.; Zhang, C.; Lai, C.; Zeng, G.; Huang, D.; Cheng, M.; Wang, J.; Chen, F.; Zhou, C.; Xiong, W. BiOX (X = Cl, Br, I) Photocatalytic Nanomaterials: Applications for Fuels and Environmental Management. *Adv. Colloid Interface Sci.* **2018**, *254*, 76−93.
(5) Xiong, J.; Song, P.; Di, J.; Li, H. Bismuth-Rich Bismuth Oxyhalides: A New Opportunity to Trigger High-Efficiency Photocatalysis. *J. Mater. Chem. A* **2020**, *8* (41), 21434−21454.
(6) Liu, B.; Wang, Y.; Chen, P.; Zhang, X.; Sun, H.; Tang, Y.; Liao, Q.; Huang, J.; Wang, H.; Meng, H.; Guo, X. Boosting Efficiency and Stability of Organic Solar Cells Using Ultralow-Cost BiOCl Nanoplates as Hole Transporting Layers. *ACS Appl. Mater. Interfaces* **2019**, *11* (36), 33505−33514.
(7) Liu, L.; Sun, Y.; Cui, X.; Qi, K.; He, X.; Bao, Q.; Ma, W.; Lu, J.; Fang, H.; Zhang, P.; Zheng, L.; Yu, L.; Singh, D. J.; Xiong, Q.; Zhang, L.; Zheng, W. Bottom-up Growth of Homogeneous Moiré Superlattices in Bismuth Oxychloride Spiral Nanosheets. *Nat. Commun.* **2019**, *10* (1), No. 4472.
(8) Crovetto, A.; Hajijafarassar, A.; Hansen, O.; Seger, B.; Chorkendorff, I.; Vesborg, P. C. K. Parallel Evaluation of the BiI_3, BiOI, and Ag_3BiI_6 Layered Photoabsorbers. *Chem. Mater.* **2020**, *32* (8), 3385−3395.
(9) Wang, L.; Wang, L.; Du, Y.; Xu, X.; Dou, S. X. Progress and Perspectives of Bismuth Oxyhalides in Catalytic Applications. *Mater. Today Phys.* **2021**, *16*, No. 100294.
(10) Sun, X.; Huang, H.; Zhao, Q.; Ma, T.; Wang, L. Thin-Layered Photocatalysts. *Adv. Funct. Mater.* **2020**, *30* (22), No. 1910005.
(11) Sridharan, K.; Shenoy, S.; Kumar, S. G.; Terashima, C.; Fujishima, A.; Pitchaimuthu, S. Advanced Two-Dimensional Heterojunction Photocatalysts of Stoichiometric and Non-Stoichiometric Bismuth Oxyhalides with Graphitic Carbon Nitride for Sustainable Energy and Environmental Applications. *Catalysts* **2021**, *11* (4), 426.
(12) Bannister, F. A. The Crystal-Structure of the Bismuth Oxyhalides. *Miner. Mag. J. Miner. Soc.* **1935**, *24* (149), 49−58.
(13) Dong, X.-D.; Zhang, Y.-M.; Zhao, Z.-Y. Role of the Polar Electric Field in Bismuth Oxyhalides for Photocatalytic Water Splitting. *Inorg. Chem.* **2021**, *60* (12), 8461−8474.
(14) Wu, Z.; Li, W.; Xu, J.; Jing, J.; Li, J.; Shen, J.; Yang, L.; Feng, W.; Zhang, S.; Zhu, Y. Internal Electric Field Enhancement by the I-Rich Surface of Highly Crystallized BiOI Nanosheets for Boosted Photocatalytic Degradation of Phenol. *Small Struct.* **2023**, *4* (9), No. 2200380.
(15) Ren, X.; Li, J.; Cao, X.; Wang, B.; Zhang, Y.; Wei, Y. Synergistic Effect of Internal Electric Field and Oxygen Vacancy on the Photocatalytic Activity of BiOBrxI1−x with Isomorphous Fluorine Substitution. *J. Colloid Interface Sci.* **2019**, *554*, 500−511.
(16) Xu, Y.; Shi, Z.; Zhang, L.; Brown, E. M. B.; Wu, A. Layered Bismuth Oxyhalide Nanomaterials for Highly Efficient Tumor Photodynamic Therapy. *Nanoscale* **2016**, *8* (25), 12715−12722.
(17) Jagt, R. A.; Bravić, I.; Eyre, L.; Gałkowski, K.; Borowiec, J.; Dudipala, K. R.; Baranowski, M.; Dyksik, M.; van de Goor, T. W. J.; Kreouzis, T.; Xiao, M.; Bevan, A.; Płochocka, P.; Stranks, S. D.; Deschler, F.; Monserrat, B.; MacManus-Driscoll, J. L.; Hoye, R. L. Z. Layered BiOI Single Crystals Capable of Detecting Low Dose Rates of X-Rays. *Nat. Commun.* **2023**, *14* (1), No. 2452.
(18) Yu, Z.; Yang, H.; Soin, N.; Chen, L.; Black, N.; Xu, K.; Sharma, P. K.; Tsonos, C.; Kumar, A.; Luo, J. Bismuth Oxyhalide Based Photo-Enhanced Triboelectric Nanogenerators. *Nano Energy* **2021**, *89*, No. 106419.
(19) Di, J.; Xia, J.; Li, H.; Guo, S.; Dai, S. Bismuth Oxyhalide Layered Materials for Energy and Environmental Applications. *Nano Energy* **2017**, *41*, 172−192.
(20) Jin, X.; Ye, L.; Xie, H.; Chen, G. Bismuth-Rich Bismuth Oxyhalides for Environmental and Energy Photocatalysis. *Coord. Chem. Rev.* **2017**, *349*, 84−101.
(21) Di, J.; Xia, J.; Ji, M.; Wang, B.; Yin, S.; Xu, H.; Chen, Z.; Li, H. Carbon Quantum Dots Induced Ultrasmall BiOI Nanosheets with Assembled Hollow Structures for Broad Spectrum Photocatalytic Activity and Mechanism Insight. *Langmuir* **2016**, *32* (8), 2075−2084.
(22) Shan, L.-W.; He, L.-Q.; Suriyaprakash, J.; Yang, L.-X. Photoelectrochemical (PEC) Water Splitting of BiOI{001} Nanosheets Synthesized by a Simple Chemical Transformation. *J. Alloys Compd.* **2016**, *665*, 158−164.
(23) Sun, Z.; Amrillah, T. Potential Application of Bismuth Oxyiodide (BiOI) When It Meets Light. *Nanoscale* **2024**, *16* (10), 5079−5106.
(24) Shi, X.; Liu, H.; Tian, J.; Ning, P.; Zhang, J.; Shi, X. Carbon-Coated BiOBr Composite Prepared by Molten Salt Method and Mechanical Ball Milling as Anode Material for Lithium-Ion Batteries. *Inorg. Chem. Commun.* **2021**, *125*, No. 108415.
(25) Li, W.; Xu, Y.; Dong, Y.; Wu, Y.; Zhang, C.; Zhou, M.; Fu, Q.; Wu, M.; Lei, Y. Bismuth Oxychloride Nanoflake Assemblies as a New Anode for Potassium Ion Batteries. *Chem. Commun.* **2019**, *55* (46), 6507−6510.
(26) Awasthi, K.; Chang, F.-L.; Hsu, H.-Y.; Ohta, N. Cancer Specific Apoptosis Induced by Electric Field: A Possible Key Mechanism in Cell-Competition and Photodynamic Action. *Sens. Actuators, B* **2021**, *347*, No. 130635.
(27) Zhao, Z.-Y.; Dai, W.-W. Electronic Structure and Optical Properties of BiOI Ultrathin Films for Photocatalytic Water Splitting. *Inorg. Chem.* **2015**, *54* (22), 10732−10737.
(28) Huq, T. N.; Lee, L. C.; Eyre, L.; Li, W.; Jagt, R. A.; Kim, C.; Fearn, S.; Pecunia, V.; Deschler, F.; MacManus-Driscoll, J. L.; Hoye, R. L. Z. Electronic Structure and Optoelectronic Properties of Bismuth Oxyiodide Robust against Percent-Level Iodine-, Oxygen-, and Bismuth-Related Surface Defects. *Adv. Funct. Mater.* **2020**, *30* (13), No. 1909983.
(29) Hou, J.; Jiang, K.; Shen, M.; Wei, R.; Wu, X.; Idrees, F.; Cao, C. Micro and Nano Hierachical Structures of BiOI/Activated Carbon for Efficient Visible-Light-Photocatalytic Reactions. *Sci. Rep.* **2017**, *7* (1), No. 11665.
(30) Tian, N.; Huang, H.; Wang, S.; Zhang, T.; Du, X.; Zhang, Y. Facet-Charge-Induced Coupling Dependent Interfacial Photocharge Separation: A Case of BiOI/g-C3N4 p-n Junction. *Appl. Catal., B* **2020**, *267*, No. 118697.
(31) Pan, M.; Zhang, H.; Gao, G.; Liu, L.; Chen, W. Facet-Dependent Catalytic Activity of Nanosheet-Assembled Bismuth Oxyiodide Microspheres in Degradation of Bisphenol A. *Environ. Sci. Technol.* **2015**, *49* (10), 6240−6248.
(32) Ye, L.; Jin, X.; Ji, X.; Liu, C.; Su, Y.; Xie, H.; Liu, C. Facet-Dependent Photocatalytic Reduction of CO2 on BiOI Nanosheets. *Chem. Eng. J.* **2016**, *291*, 39−46.
(33) Prasad, M. D.; Krishna, M. G.; Batabyal, S. K. Facet-Engineered Surfaces of Two-Dimensional Layered BiOI and Au−BiOI Substrates for Tuning the Surface-Enhanced Raman Scattering and Visible Light Photodetector Response. *ACS Appl. Nano Mater.* **2019**, *2* (6), 3906−3915.
(34) Wu, J.; Chen, X.; Li, C.; Qi, Y.; Qi, X.; Ren, J.; Yuan, B.; Ni, B.; Zhou, R.; Zhang, J.; Huang, T. Hydrothermal Synthesis of Carbon Spheres − BiOI/BiOIO3 Heterojunctions for Photocatalytic Removal of Gaseous Hg0 under Visible Light. *Chem. Eng. J.* **2016**, *304*, 533−543.
(35) Wang, X.; Li, Q.; Zhou, C.; Zhang, R. Iodine-Vacancy BiOI1-x Ultrathin Sheets for Improved Visible-Light Photooxidation Activities. *Appl. Surf. Sci.* **2019**, *493*, 657−664.
(36) Zeng, W.; Li, J.; Feng, L.; Pan, H.; Zhang, X.; Sun, H.; Liu, Z. Synthesis of Large-Area Atomically Thin BiOI Crystals with Highly Sensitive and Controllable Photodetection. *Adv. Funct. Mater.* **2019**, *29* (16), No. 1900129.
(37) Ye, L.; Zan, L.; Tian, L.; Peng, T.; Zhang, J. The {001} Facets-Dependent High Photoactivity of BiOCl Nanosheets. *Chem. Commun.* **2011**, *47* (24), 6951−6953.
(38) Wang, Z.; Chu, Z.; Dong, C.; Wang, Z.; Yao, S.; Gao, H.; Liu, Z.; Liu, Y.; Yang, B.; Zhang, H. Ultrathin BiOX (X = Cl, Br, I)

https://doi.org/10.1021/acsanm.4c06892
ACS Appl. Nano Mater. 2025, 8, 4017−4025

Nanosheets with Exposed {001} Facets for Photocatalysis. *ACS Appl. Nano Mater.* **2020**, *3* (2), 1981−1991.
(39) Hou, J.; Jiang, T.; Wei, R.; Idrees, F.; Bahnemann, D. Ultrathin-Layer Structure of BiOI Microspheres Decorated on N-Doped Biochar With Efficient Photocatalytic Activity. *Front. Chem.* **2019**, *7*, No. 378.
(40) Xu, Z.; Hao, W.; Zhang, Q.; Fu, Z.; Feng, H.; Du, Y.; Dou, S. Indirect-Direct Band Transformation of Few-Layer BiOCl under Biaxial Strain. *J. Phys. Chem. C* **2016**, *120* (16), 8589−8594.
(41) Barhoumi, M.; Said, M. Electronic and Optical Properties of Bismuth Oxyhalides from Ab Initio Calculations. *Mater. Sci. Eng. B* **2021**, *264*, No. 114921.
(42) Weng, S.; Pei, Z. X.; Zheng, Z.; Hu, J.; Liu, P. Exciton-Free, Nonsensitized Degradation of 2-Napthol by Facet-Dependent BiOCl under Visible Light: Novel Evidence of Surface-State Photocatalysis. *ACS Appl. Mater. Interfaces* **2013**, *5* (23), 12380−12386.
(43) Xiong, X.; Ding, L.; Wang, Q.; Li, Y.; Jiang, Q.; Hu, J. Synthesis and Photocatalytic Activity of BiOBr Nanosheets with Tunable Exposed {010} Facets. *Appl. Catal., B* **2016**, *188*, 283−291.
(44) Li, B.; Shao, L.; Zhang, B.; Wang, R.; Zhu, M.; Gu, X. Understanding Size-Dependent Properties of BiOCl Nanosheets and Exploring More Catalysis. *J. Colloid Interface Sci.* **2017**, *505*, 653−663.
(45) Han, A.; Sun, J.; Lin, X.; Yuan, C.-H.; Chuah, G. K.; Jaenicke, S. Influence of Facets and Heterojunctions in Photoactive Bismuth Oxyiodide. *RSC Adv.* **2015**, *5* (107), 88298−88305.
(46) Jiang, J.; Zhao, K.; Xiao, X.; Zhang, L. Synthesis and Facet-Dependent Photoreactivity of BiOCl Single-Crystalline Nanosheets. *J. Am. Chem. Soc.* **2012**, *134* (10), 4473−4476.
(47) He, Y.; Men, D.; Pang, Y.; Guo, H.; Gu, J.; Li, A. Sample Fabrication of BiOCl Nanosheets with Low Specific Surface Area for Efficient Photocatalytic Degradation of Organic Wastewater. *Langmuir* **2024**, *40* (32), 16900−16908.
(48) Fan, W.; Li, H.; Zhao, F.; Xiao, X.; Huang, Y.; Ji, H.; Tong, Y. Boosting the Photocatalytic Performance of (001) BiOI: Enhancing Donor Density and Separation Efficiency of Photogenerated Electrons and Holes. *Chem. Commun.* **2016**, *52*, 5316−5319.
(49) Xiao, Y.; Wu, J.; Jia, T.; Li, T.; Wang, Z.; Qi, Y.; Liu, Q.; Qi, X.; He, P. Fabrication of BiOI Nanosheets with Exposed (001) and (110) Facets with Different Methods for Photocatalytic Oxidation Elemental Mercury. *Colloid Interface Sci. Commun.* **2021**, *40*, No. 110357.
(50) Bhosale, A. H.; Narra, S.; Bhosale, S. S.; Liao, P.-S.; Ohta, N.; Diau, E. W.-G. Femtosecond Relaxation Dynamics of Two-dimensional BiOI Nanoplatelets as Efficient Photocatalysts. *J. Chin. Chem. Soc.* **2022**, *69* (1), 51−59.
(51) Florez-Rios, J. F.; Santana-Aranda, M. A.; Quiones-Galvn, J. G.; Escobedo-Morales, A.; Chvez-Chvez, A.; Prez-Centeno, A. Alternative Bi Precursor Effects on the Structural, Optical, Morphological and Photocatalytic Properties of BiOI Nanostructures. *Mater. Res. Express* **2020**, *7* (1), No. 015912.
(52) Bublitz, G. U.; Boxer, S. G. STARK SPECTROSCOPY: Applications in Chemistry, Biology, and Materials Science. *Annu. Rev. Phys. Chem.* **1997**, *48* (1), 213−242.
(53) Liptay, W. Dipole Moments and Polarizabilities of Molecules in Excited Electronic States. In *Excited States*; Lim, E. C., Ed.; Academic Press: New York, 1974; pp 129−229.
(54) Jalviste, E.; Ohta, N. Theoretical Foundation of Electroabsorption Spectroscopy: Self-Contained Derivation of the Basic Equations with the Direction Cosine Method and the Euler Angle Method. *J. Photochem. Photobiol. C: Photochem. Rev.* **2007**, *8* (1), 30−46.
(55) Bothra, U.; Westbrook, R. J. E.; Liu, Y.; Wang, J.; Ziffer, M. E.; Ginger, D. S. Probing Charge Transfer Character in Modern Donor/Acceptor Materials via Electroabsorption Spectroscopy. *J. Phys. Chem. Lett.* **2024**, *15* (5), 1288−1293.
(56) Islam, A.; Kikuchi, Y.; Iimori, T. Electroabsorption and Stark Fluorescence Spectroscopies of Thioflavin T. *J. Phys. Chem. A* **2023**, *127* (6), 1436−1444.
(57) Hamada, M.; Rana, S.; Jokar, E.; Awasthi, K.; Diau, E. W.-G.; Ohta, N. Temperature-Dependent Electroabsorption Spectra and Exciton Binding Energy in a Perovskite CH3NH3PbI3 Nanocrystalline Film. *ACS Appl. Energy Mater.* **2020**, *3* (12), 11830−11840.
(58) Awasthi, K.; Iimori, T.; Ohta, N. Integral Method Analysis of Electroabsorption Spectra and Its Application to Quantum Dots of PbSe. *J. Phys. Chem. C* **2014**, *118* (31), 18170−18176.
(59) Kattoor, V.; Awasthi, K.; Jokar, E.; Diau, E. W.-G.; Ohta, N. Integral Method Analysis of Electroabsorption Spectra and Electrophotoluminescence Study of (C4H9NH3)2Pbl4 Organic−Inorganic Quantum Well. *J. Phys. Chem. C* **2018**, *122* (46), 26623−26634.
(60) Rieger, S.; Fürmann, T.; Stolarczyk, J. K.; Feldmann, J. Optically Induced Coherent Phonons in Bismuth Oxyiodide (BiOI) Nanoplatelets. *Nano Lett.* **2021**, *21* (18), 7887−7893.
(61) Gosztola, D.; Yamada, H.; Wasielewski, M. R. Electric Field Effects of Photogenerated Ion Pairs on Nearby Molecules: A Model for the Cartenoid Band Shift in Photosynthesis. *J. Am. Chem. Soc.* **1995**, *117* (7), 2041−2048.
(62) Huang, W. L. Electronic Structures and Optical Properties of BiOX (X = F, Cl, Br, I) via DFT Calculations. *J. Comput. Chem.* **2009**, *30* (12), 1882−1891.
(63) Zhang, H.; Liu, L.; Zhou, Z. Towards Better Photocatalysts: First-Principles Studies of the Alloying Effects on the Photocatalytic Activities of Bismuth Oxyhalides under Visible Light. *Phys. Chem. Chem. Phys.* **2012**, *14* (3), 1286−1292.
(64) Liu, Y.; Zhou, T.; Zheng, Y.; He, Z.; Xiao, C.; Pang, W. K.; Tong, W.; Zou, Y.; Pan, B.; Guo, Z.; Xie, Y. Local Electric Field Facilitates High-Performance Li-Ion Batteries. *ACS Nano* **2017**, *11* (8), 8519−8526.
(65) Shi, X.; Li, J.; Zhang, X.; Li, M.; Jing, Q.; Fang, G.; Long, M. Utilizing the Built-In Electric Field of SnS2/C3N Heterostructure to Promote High-Performance Lithium-Ion Batteries. *J. Phys. Chem. C* **2024**, *128* (15), 6189−6197.
(66) Umeuchi, S.; Nishimura, Y.; Yamazaki, I.; Murakami, H.; Yamashita, M.; Ohta, N. Electric Field Effects on Absorption and Fluorescence Spectra of Pyrene Doped in a PMMA Polymer Film. *Thin Solid Films* **1997**, *311* (1−2), 239−245.
(67) Mehata, M. S.; Hsu, C.-S.; Lee, Y.-P.; Ohta, N. Electric Field Effects on Photoluminescence of Polyfluorene Thin Films: Dependence on Excitation Wavelength, Field Strength and Temperature. *J. Phys. Chem. C* **2009**, *113* (27), 11907−11915.

https://doi.org/10.1021/acsanm.4c06892
ACS Appl. Nano Mater. 2025, 8, 4017−4025